DOI: 10.61782/fa.2023.0839

forum acusticum 2023

FREQUENCY-INDEPENDENT HOMOGENISED ELASTIC AND DAMPING CONSTANTS OF CROSS-LAMINATED TIMBER

Sven Vallely[1*] **Stefan Schoenwald**[1]
[1] Laboratory for Acoustics / Noise Control
Swiss Federal Laboratories for Materials Science and Technology (Empa)

ABSTRACT

Engineered wood elements are composite elements that are widely used all over the world for the construction of multi-storey wooden buildings due to their favourable stiffness-to-mass-density ratio. However, this favourable structural design property is generally in contrast to properties that facilitate good vibro-acoustic performance. Fortunately, the properties of such composite elements can be tailored by adjusting the dimensions, orientations, stacking sequences, and constitutive materials of the wooden layers that are glued together. This array of additional parameters associated with composite structures allows for additional design degrees of freedom to overcome contrasting design requirements. To explore this extended design space effectively, efficient and extensible models are required; however, a major challenge for such models is the inhomogeneous and anisotropic nature of engineered wood elements. A step towards achieving efficient and extensible models is the homogenisation of such elements. So far, broadband homogenisation approaches have relied on frequency-dependent material properties. This contribution presents an experimental validation of a method for deriving frequency-independent elastic and damping constants for cross-laminated timber and a discussion of the associated limitations of these frequency-independent constants for broadband use in building acoustics.

Keywords: *Homogenisation,Homogenization,Cross-Laminated Timber,CLT*

**Corresponding author*: *sven.vallely@empa.ch.*

1. INTRODUCTION

Cross-Laminated Timber (CLT) is a renewable and environmentally friendly engineered wood product. CLT has already shown potential as an alternative stand-alone structural element to established construction materials derived from mineral resources, such as concrete and steel. This is due to CLT's relatively high stiffness-to-mass-density ratio as a building element. However, while this property correlates positively with static structural requirements, the same property correlates negatively with noise and vibration requirements.

Further challenges in the implementation of CLT as a structural element are the orthotropic nature of wood, a constituent material, and the overall inhomogeneous nature of the structural element. These characteristics lead to more complex mechanical behaviour, posing additional challenges over standard isotropic and homogeneous materials, such as steel. However, this general anisotropic and inhomogeneous nature of CLT also provides additional design degrees of freedom, which can be utilised to overcome competing design requirements.

Before these additional design degrees of freedom can be fully utilised, analytical methods and numerical simulation models for the analysis of CLT need to be developed. One such approach in the vibro-acoustic analysis of CLT is the homogenisation of the structural element to be represented by an Equivalent Single Layer (ESL). A macromechanical method to obtain broadband frequency-independent homogenised material properties for such an ESL is presented in [1].

This contribution provides further experimental validation of the analytical methods and numerical mod-

els presented in [1] for deriving frequency-independent elastic and damping constants of CLT and discusses the limitations of using such constants for broadband vibro-acoustic models. In this contribution, broadband is defined in the context of building acoustics, where the frequency range of interest is typically up to the upper bound of the nominal 3150 Hz one-third octave band [2].

2. BACKGROUND AND THEORY

2.1 Harmonic Analysis

The system is analysed under the excitation of forced harmonic vibrations with hysteretic damping. The equation of motion is [3]

$$\mathbf{M}\ddot{\mathbf{u}} + \mathbf{K}\left(1 + i\eta\right)\mathbf{u} = \mathbf{F}, \tag{1}$$

where $\mathbf{K}$ and $\mathbf{M}$ are the stiffness and mass matrices of the system, respectively. $\mathbf{u}$ and $\ddot{\mathbf{u}}$ are the respective displacement and acceleration vectors of the system, and η is the structural damping loss factor of the system. $\mathbf{F}$ is the vector of externally applied loads which may be a combination of frequency-dependent harmonic and static loads.

2.2 Homogenisation

The homogenisation theory applied in this contribution is based on an augmented classical lamination theory that includes first-order shear deformations with shear correction factors derived from the actual shear stress distribution of the considered laminate. The homogenised properties are given in stiffness or compliance matrix form [1],

$$\begin{bmatrix} \boldsymbol{\varepsilon} \\ \boldsymbol{\kappa} \\ \boldsymbol{\gamma} \end{bmatrix} = \begin{bmatrix} \mathbf{a} & \mathbf{b} & \mathbf{0} \\ \mathbf{b} & \mathbf{d} & \mathbf{0} \\ \mathbf{0} & \mathbf{0} & \widetilde{\mathbf{h}} \end{bmatrix} \begin{bmatrix} \mathbf{N} \\ \mathbf{M} \\ \mathbf{V} \end{bmatrix}, \tag{2}$$

from which uncoupled flexural or planar engineering constants can be deduced. A full derivation is given in [1].

2.3 Spatially Averaged Squared Transfer Mobility

For broadband response comparisons in vibro-acoustics, the spatial average of the square of the surface response velocity $\overline{|v|^2}$ is used rather than dealing with the details of all of the eigenmodes and their respective eigenfrequencies and damping factors. $\overline{|v|^2}$ is defined as [4]

$$\overline{|v|^2} = \frac{1}{m_{tot}} \iint \rho_A(x,y)|v(x,y)|^2 \,\mathrm{d}x\mathrm{d}y, \tag{3}$$

where m_{tot} is the total mass, $\rho_A(x,y)$ is the area density, and $v(x,y)$ is the complex velocity distribution of the vibrating system. $\overline{|v|^2}$ is the approximate total energy of the vibrating system divided by the total mass of the system at resonance where bending waves are dominant.

In order to compare $\overline{|v|^2}$ across different studies, $\overline{|v|^2}$ is normalised by the square of the modulus of the respective point excitation force F_i to derive the spatially averaged squared transfer mobility $\overline{|Y|^2}$,

$$\overline{|Y(\omega)|^2} = \frac{\overline{|v(\omega)|^2}}{|F_i(\omega)|^2}. \tag{4}$$

2.4 Power Injection Method

A means for determining an averaged loss factor of a vibrating structural system is the power injection method [4, 5]. The power injection method approximates the loss factor η of the system by the ratio of the dissipated energy E_{diss} to the maximum strain energy E_V of the system per radian under steady-state vibration [4],

$$\eta = \frac{E_{diss}}{2\pi E_V}. \tag{5}$$

Assuming the input force consists of a stationary signal and remains fixed at a location, the energy dissipated is equivalent to the energy input into the system [4, 5],

$$E_{diss} = E_{in}. \tag{6}$$

The energy input into the system can be derived at a given frequency from the power input into the system, W_{in} (input force multiplied by velocity at the point of excitation, determined from the cross power spectrum), multiplied by the period of the given cycle T [4],

$$E_{in} = W_{in}T. \tag{7}$$

The total strain energy can be approximated from the total kinetic energy of the system. An approximation that is valid at resonance or when considering an average across many resonances in a given frequency band. The total kinetic energy for a uniform plate can be calculated from the spatially averaged squared velocity response of the system presented in Eqn. (3) [4],

$$E_V = E_T = \frac{1}{2}m\overline{|v|^2}. \tag{8}$$

Substituting Eqn. (6), Eqn. (7), and Eqn. (8) into Eqn. (5), the loss factor is defined by terms that can be conveniently determined in situ:

$$\eta = \frac{2W_{in}}{\omega m \overline{|v|^2}}. \tag{9}$$

3. MATERIALS AND METHODS

3.1 Test Specimens

The test specimens considered were two 5-ply CLT plates with $[0/90/0/90/0]$ lay-up (or concisely, $[0/90/\overline{0}]_s$) and plies of $40\,\mathrm{mm}$ thickness each. Both specimens had a $5.73\,\mathrm{m} \times 0.100\,\mathrm{m} \times 0.100\,\mathrm{m}$ notch for a half-lap joint along one side. The geometrical properties of the plates are given in Tab. 1.

Table 1: Identification (ID) of the experimentally investigated plates by geometrical properties. Namely length a, width b, total thickness t_{tot}, lay-up, and layer thickness t_i.

Plate ID	a (m)	b (m)	t_{tot} (m)	Lay-up (°)	t_i (mm)
CLT200a	5.73	2.38	0.200	$[0/90/\overline{0}]_s$	40
CLT200b		2.28			

3.2 Experimental Set-up and Measurement

Both plates had similar experimental set-ups, supported on three air jacks while they were excited on the underside with a shaker and scanned from above with a Polytec PSV-400 laser Doppler vibrometer. A photo of the experimental set-up with CLT200b is presented in Fig. 1. A photo of the experimental set-up for CLT200a can be found in [1]. CLT200a was excited with a Data Physics IV40 inertial shaker, while CLT200b was excited with a Bruel and Kjaer LSD V201 modal shaker. At their respective excitation points, both plates had a PCB 288D01 impedance head attached, to which the respective shakers were attached.

The excitation signal was a swept sine from $16\,\mathrm{Hz}$ to $6600\,\mathrm{Hz}$ for CLT200a and from $15\,\mathrm{Hz}$ to $5500\,\mathrm{Hz}$ for CLT200b. The approximate excitation locations for each plate are depicted in Fig. 2 and the relative excitation locations are given in Tab. 2.

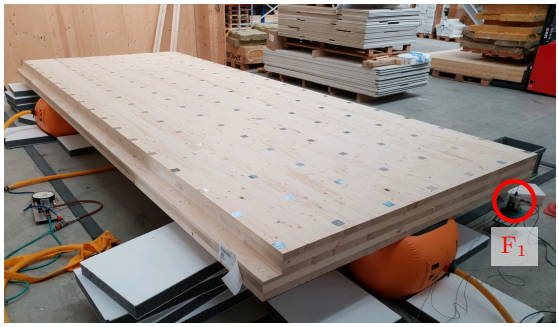

Figure 1: Photo of the experimental set-up for plate CLT200b with shaker located at the F_1 excitation point.

Table 2: Excitation point locations on the plane with respect to the nearest short edge $\Delta \mathrm{x_b}$ and long edge $\Delta \mathrm{y_a}$.

Plate ID	Exc. Point	$\Delta \mathrm{x_b}$ (cm)	$\Delta \mathrm{y_a}$ (cm)
CLT200a	F_1	4.00	5.00
	F_2	9.00	13.0
	F_3	3.00	114
CLT200b	F_1	4.00	5.00
	F_2	9.00	13.0
	F_3	3.00	109

For CLT200a, the measurement grid was a rectangular 16×39 grid of points, corresponding to a spatial resolution of approximately $15\,\mathrm{cm}$. For CLT200b, the measurement grid was a 7×18 grid of points, corresponding to a spatial resolution of approximately $34\,\mathrm{cm}$. The approximate measurement grids of the plates are depicted in Fig. 2. Time sampling parameters of the measured signals were chosen to obtain FFT data with frequency resolutions of $62.5\,\mathrm{mHz}$ and $195\,\mathrm{mHz}$ for CLT200a and CLT200b, respectively.

3.3 Material Property Derivation

3.3.1 Mass Density

Both plates were weighed, and the difference in their derived mass densities was less than $1\,\%$.

3.3.2 Damping

The structural damping loss factor was derived on a one-third octave band basis from the experimental

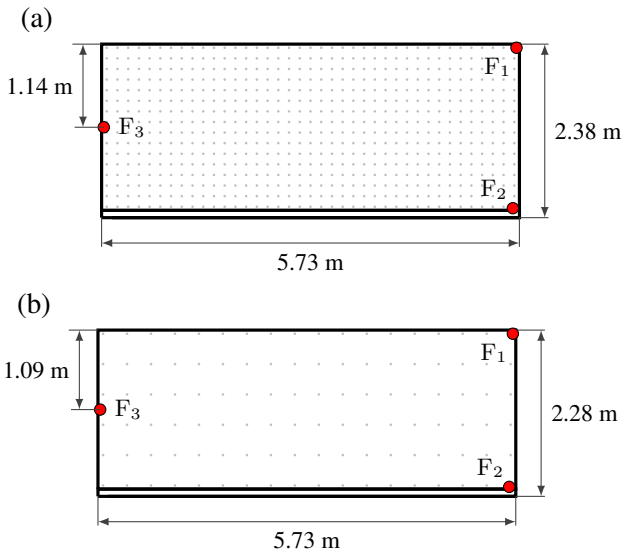

Figure 2: Schematic indicating planar dimensions, approximate measurement grid, and locations of the excitation positions for plates: (a) CLT200a and (b) CLT200b.

measurements using Eqn. (9). The spatially averaged mean square velocity was obtained from the laser Doppler vibrometer measurements, and the power injected was determined from the cross-spectrum of the force and acceleration signal of the impedance head at the respective excitation points of the plates. The average loss factor of the two plates is presented in Fig. 3. The loss factor is only presented for bands with eigenfrequencies present. A frequency-independent loss factor is derived by averaging from 100 Hz to 1600 Hz. This range selects for one-third octave bands which have a modal density of two or higher and are not influenced by thickness-stretch resonances.

In general, the calculated loss factor captures not only internal mechanisms of damping but also external mechanisms, such as losses due to interaction with the air jacks and acoustic radiation. It is, however, assumed that these external damping mechanisms are negligible. Therefore, the derived loss factor is assumed to represent the internal losses of the system.

3.3.3 Engineering Constants

The layerwise material properties used in this study were derived from a model updating process based on the extracted eigenmodes and associated eigenfrequencies of CLT200a [1]. For the ESL, the in-plane flexural engineering constants are derived from the normalised bending compliance matrix $\mathbf{d}^*$ and the out-of-plane shear moduli are derived from the normalised corrected shear compliance matrix $\widetilde{\mathbf{h}}^*$ [1]. The remaining engineering constants are derived based on the assumptions discussed in [1]. The layerwise and ESL properties are presented in Tab. 3.

Table 3: Layerwise and ESL properties of the CLT plates.

Property	Units	Model	
		Layerwise	ESL
Lay-up	°	$[0/90/\overline{0}]_s$	[0]
Layer Thickness	mm	40	200
Total Thickness	mm	..... 200	
Loss Factor, η	1	.... 0.0170	
Density, ρ	$\mathrm{kg \cdot m^{-3}}$	..... 444	
Elastic Moduli			
E_x	GPa	11.8	9.56
E_y	GPa	0.999	3.25
E_z	GPa	.... 0.550	
Poisson's Ratios			
ν_{xy}	1	0.0100	0.0308
ν_{yz}	1	.... 0.300	
ν_{xz}	1	0.0100	0.0308
Shear Moduli [a]			
G_{xy}	GPa	.... 0.748	
G_{yz}	GPa	0.176	0.158
G_{xz}	GPa	0.538	0.229

[a] The corrected shear moduli are presented for the ESL.

3.4 Forced Response Analysis

A harmonic analysis with hysteretic damping was conducted using Ansys Mechanical, release 2022 R2. Solid rectangular prism volume ESL models were created for both of the plates using the dimensions given in Tab. 1, that is $5.73\,\mathrm{m} \times 2.38\,\mathrm{m} \times 0.200\,\mathrm{m}$ and $5.73\,\mathrm{m} \times 2.28\,\mathrm{m} \times 0.200\,\mathrm{m}$ for CLT200a and CLT200b, respectively. The half-lap joint notch seen in Fig. 1 and Fig. 2 was not modelled. The solid models were meshed

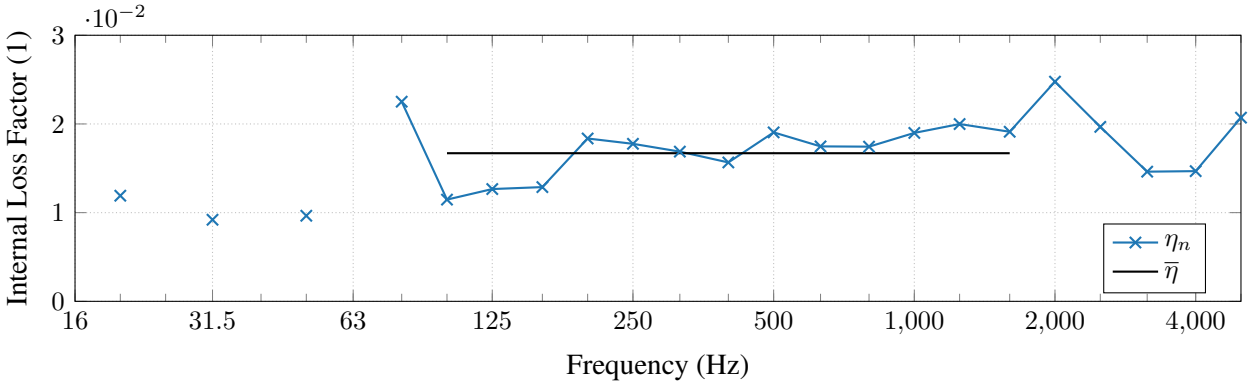

Figure 3: Average internal loss factor. η_n: Per one-third octave band. $\overline{\eta}$: Averaged from 100 Hz to 1600 Hz, $\overline{\eta} = 0.0167$.

with the Ansys SOLSH190 element, an 8-node structural solid-shell element. The meshes were mapped hexahedral meshes with a global size of 20 mm. An orthotropic material definition with the ESL material properties from Tab. 3 was assigned to both of the models. The default Ansys key options were used for the considered element, except for the shear correction factors being set to 1, since the ESL values presented in Tab. 3 already have the respective shear correction factors applied.

The analysis was conducted with free boundary conditions under the assumption that the air jacks did not influence the response of the respective plates. The swept sine excitation from the inertial shaker was modelled as a harmonic point excitation on the node nearest to the respective excitation locations. The harmonic response was calculated using the full solution method with logarithmic frequency intervals from $f_b = 6$ Hz to $f_e = 5657$ Hz with $n = 1100$ substeps. A 1 N input excitation force was used in order to obtain the transfer mobilities directly.

For post-processing, the velocity responses were mapped to the experimental measurement grids of the respective plates before calculating the respective spatially averaged squared transfer mobilities.

4. RESULTS AND DISCUSSION

A comparison of the numerical and experimental spatially averaged squared transfer mobilities expressed in terms of the sound level equivalent quantity, $L_{\overline{|Y|^2}}$, are presented in Fig. 4 and Fig. 5 for CLT200a and CLT200b, respectively. For the experimental results, $L_{\overline{|Y|^2}}$ is calculated from the 'H_1' transfer function. For both CLT200a and CLT200b, there is generally a good overall agreement between the experimental and numerical transfer mobilities for all of the considered excitation points. The largest deviations between the experimental results occur in the low- and high-frequency regions. Specifically below 100 Hz at the second and fourth resonances and in the region of 2500 Hz, where the first thickness-stretch resonance occurs.

The deviations at low frequencies are mainly due to the use of a constant loss factor for the numerical model. As is clear from Fig. 3, the one-third octave band averaged loss factors for the eigenmodes below 200 Hz have larger deviations from the calculated mean. These deviations are quantified in Fig. 6. In Fig. 6, the difference due to the assumption of a constant loss factor is compared to the actual average difference between simulation and experiment at resonance. The one-third octave band differences due to the assumption of a constant loss factor are analytically calculated from the data presented in Fig. 3 and the relation of $\overline{|v|^2}$ being proportional to $1/\eta^2$ at resonance [1, 4]. The actual difference is calculated by the average of the $L_{\overline{|Y|^2}}$ differences between simulation and experiment at resonance from the data presented in Fig. 4 and Fig. 5 for the first five resonance peaks. The values for the resonances associated with eigenmodes one (ψ_1), three (ψ_3), and five (ψ_5) are excluded for excitation point F_3 for both of the specimens due to F_3 lying on or near nodes of these eigenmodes and so not exciting these particular eigenmodes efficiently. Comparing the actual $L_{\overline{|Y|^2}}$ difference and the difference due to the assumption of a constant loss factor, the majority of the differences in the model at low frequencies can be attributed to the as-

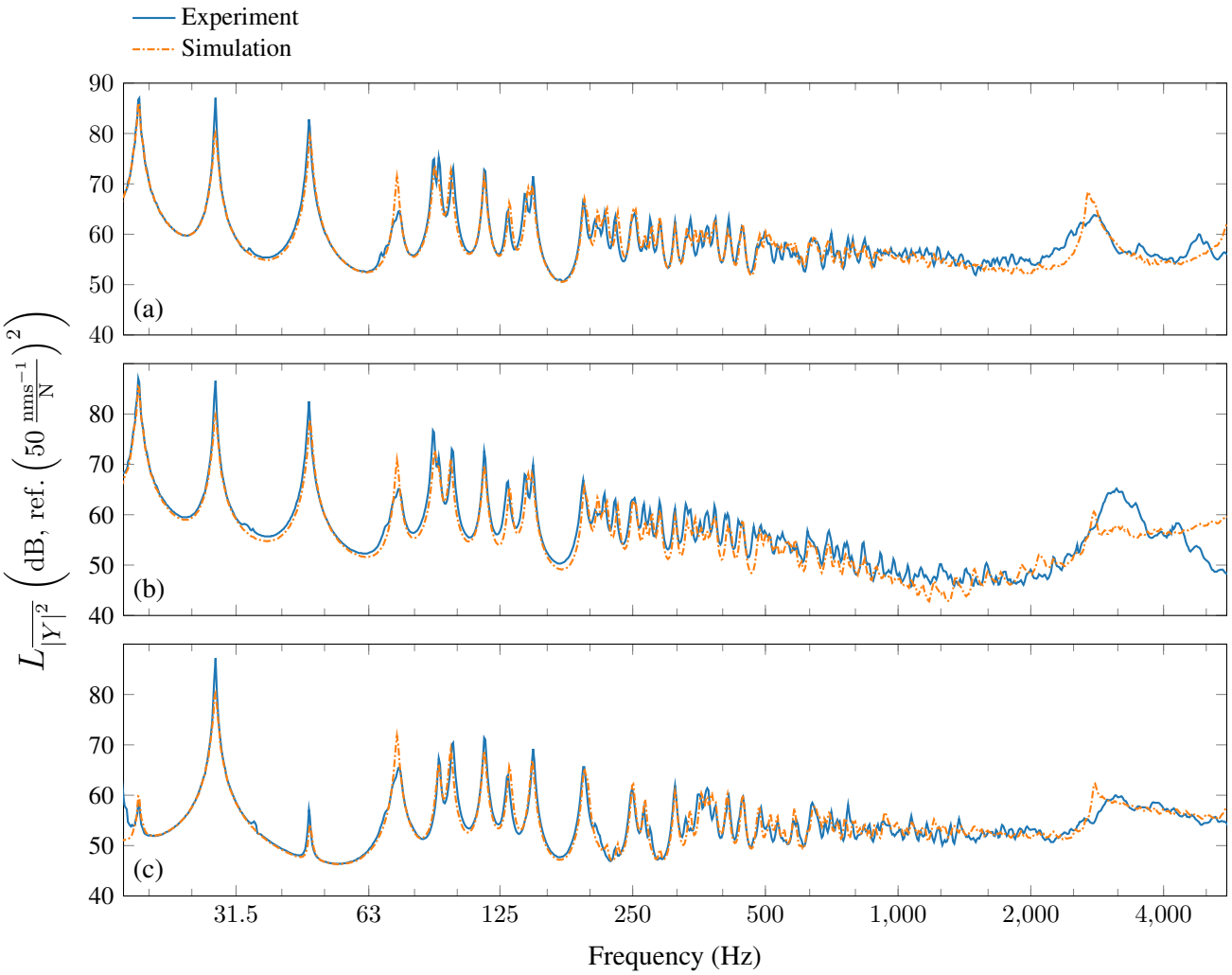

Figure 4: Spatially averaged squared transfer mobility level $\left(L_{\overline{|Y|^2}}\right)$ comparison for CLT200a. The experimental and numerical levels are presented on a base-10 logarithmic scale for excitation points (a) F_1, (b) F_2, and (c) F_3.

sumption of a constant loss factor. An exception is likely the 80 Hz one-third octave band which contains the fourth eigenmode (ψ_4). It is thought the higher loss factor of this eigenmode may be due to interaction with the air jacks, whereby the air jacks act as a vibration absorber.

The deviations at higher frequencies in Fig. 4 and Fig. 5 where the first thickness-stretch resonance cuts on, may partially be due to the use of a constant loss factor. However, a source of difference would also lie in the method used to calculate the loss factor presented in Sec. 2.4. This is due to the calculation of the maximum strain energy of the system being approximated as proportional to the spatial average of the square of the surface velocity. This assumption only holds when the infinitesimal elements are moving uniformly through the thickness of the plates, that is when no thickness-stretch modes are present. However, other sources of error, such as the global mesh size being limited by available computational resources and uncertainties in the measurement results, as the measurement set-up was optimized for the lower frequency range, are likely more significant sources of error.

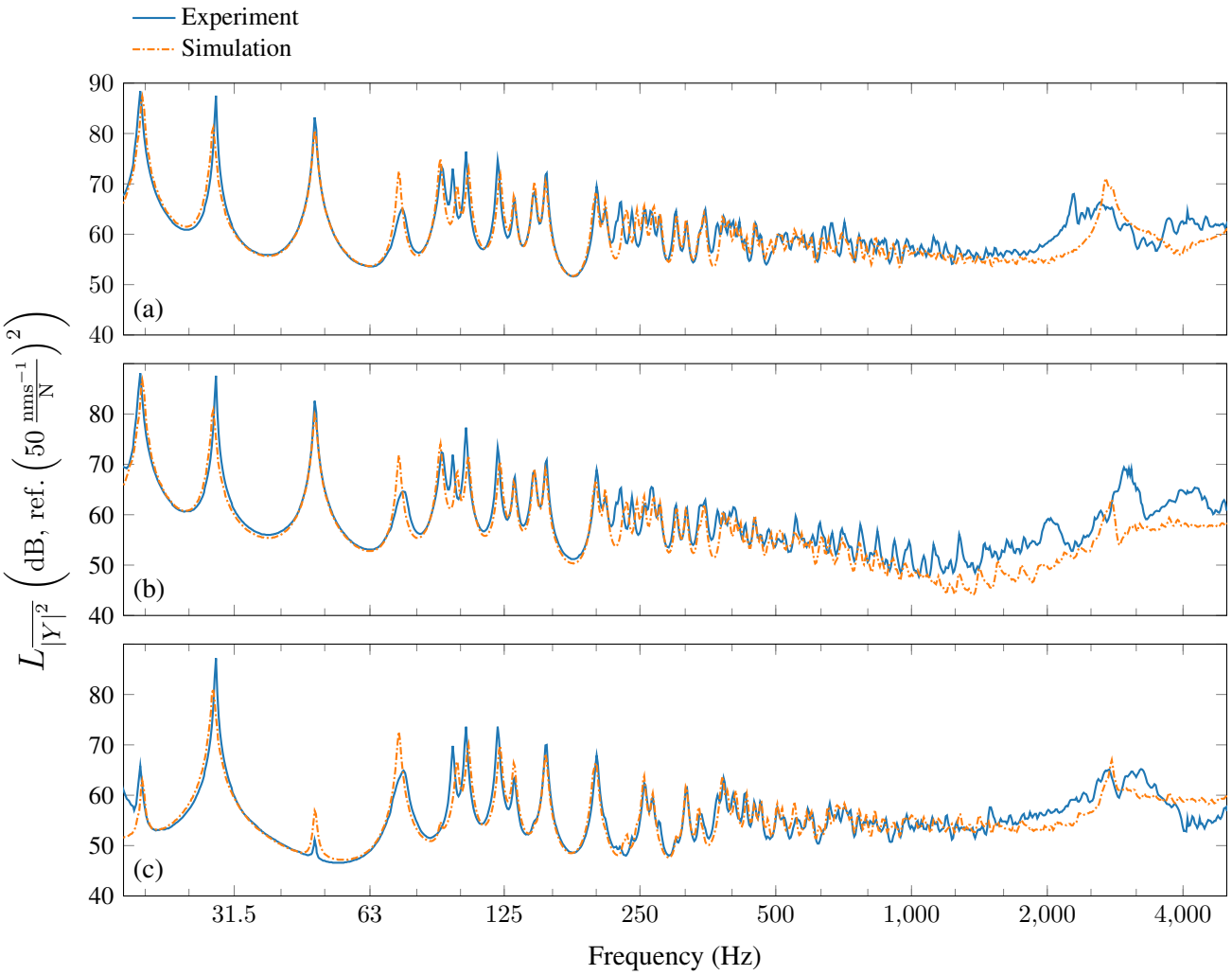

Figure 5: Spatially averaged squared transfer mobility level $\left(L_{\overline{|Y|^2}}\right)$ comparison for CLT200b. The experimental and numerical levels are presented on a base-10 logarithmic scale for excitation points (a) F_1, (b) F_2, and (c) F_3.

Another observable detail from the results presented in Fig. 4 and Fig. 5 is that excitation point F_2 has the worst agreement of the three excitation points for both of the plates. This is likely because the notches in each of the plates were not modelled. An idea supported by the larger deviations at higher frequencies, likely as the wavelength is approaching the size of the notch.

Overall, Fig. 4 and Fig. 5 show a good general agreement between the ESL CLT model and experimental results. A frequency-dependent loss factor in the model could compensate for the majority of the differences found below 200 Hz. Differences found at high frequencies may not be due to the assumption of frequency-independent material properties, but the measurement set-up and mesh size of the numerical model.

5. CONCLUSION

This contribution presents further evidence of the adequacy of frequency-independent homogenised material properties for the vibro-acoustic analysis of

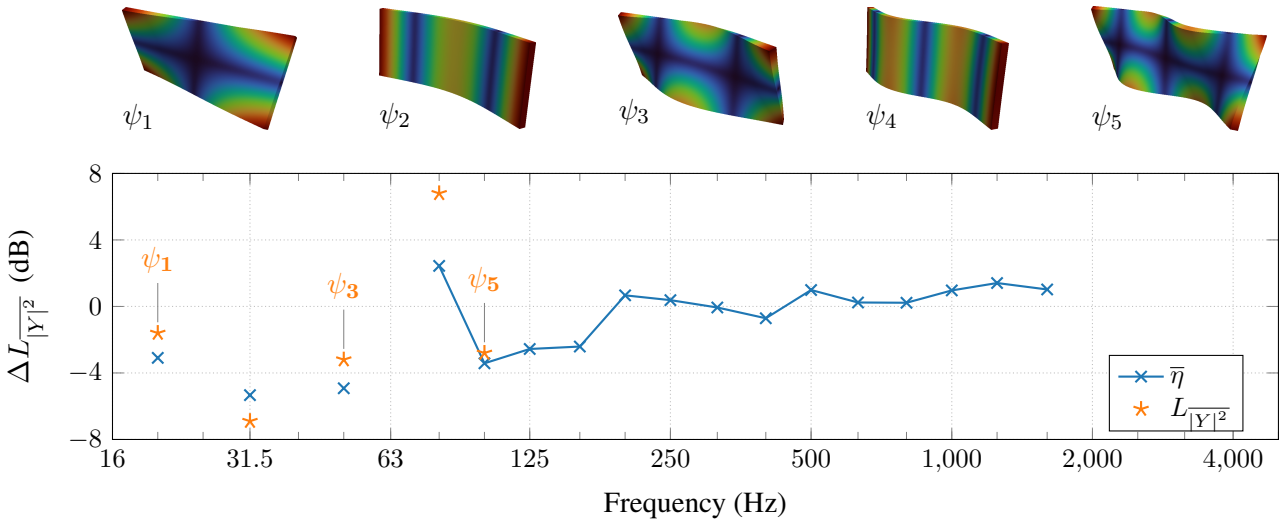

Figure 6: Average one-third octave band spatially averaged transfer mobility difference, $\Delta L_{\overline{|Y|^2}}$. $\overline{\eta}$: Due to the assumption of constant internal loss factor. $L_{\overline{|Y|^2}}$: Actual average difference for the first five eigenmodes.

cross-laminated timber elements. Flexural equivalent single-layer engineering constants are derived from layer-wise material engineering constants based on first-order shear deformation theory and utilised with an equivalent single-layer solid-shell finite element model. A good broadband agreement in the context of building acoustics is demonstrated between experimental and simulated spatially averaged square transfer mobility levels.

A next step in improving the accuracy of the model would be to implement different loss factor values over two or potentially three frequency ranges. These regions could be divided up based on modal density and when the first thickness-stretch eigenmodes cut-on. Meshing constraints due to available computational resources at the time of writing also had an effect on the accuracy of the model at high frequencies. However, this constraint could be overcome with the use of analytical or meshfree methods rather than mesh-based methods. Beyond these improvements, further significant improvements would potentially require further statistical analysis, such as quantifying uncertainties in experimental results and a move from deterministic to statistical numerical models.

6. ACKNOWLEDGEMENTS

The authors gratefully acknowledge the financial support of the research project by the Swiss Federal Office for the Environment under its Environmental Technology Promotion program and Markus Haselbach for his valuable assistance with the experimental set-up.

7. REFERENCES

[1] S. Vallely and S. Schoenwald, "An efficient analytical method to obtain the homogenised frequency-independent elastic material properties of cross-laminated timber elements," *Journal of Sound and Vibration*, vol. 546, p. 117424, 2023.

[2] C. Hopkins, *Sound insulation*. Routledge, 1st ed., 2007.

[3] A. G. Piersol and T. L. Paez, *Harris' shock and vibration handbook*. New York: McGraw-Hill, 6th ed., 2010.

[4] L. Cremer and M. Heckl, *Structure-borne sound: structural vibrations and sound radiation at audio frequencies*. Berlin, Heidelberg: Springer Science & Business Media, 2005.

[5] B. C. Bloss and M. D. Rao, "Estimation of frequency-averaged loss factors by the power injection and the impulse response decay methods," *The Journal of the Acoustical Society of America*, vol. 117, pp. 240–249, 01 2005.